[Supplementary Figures]

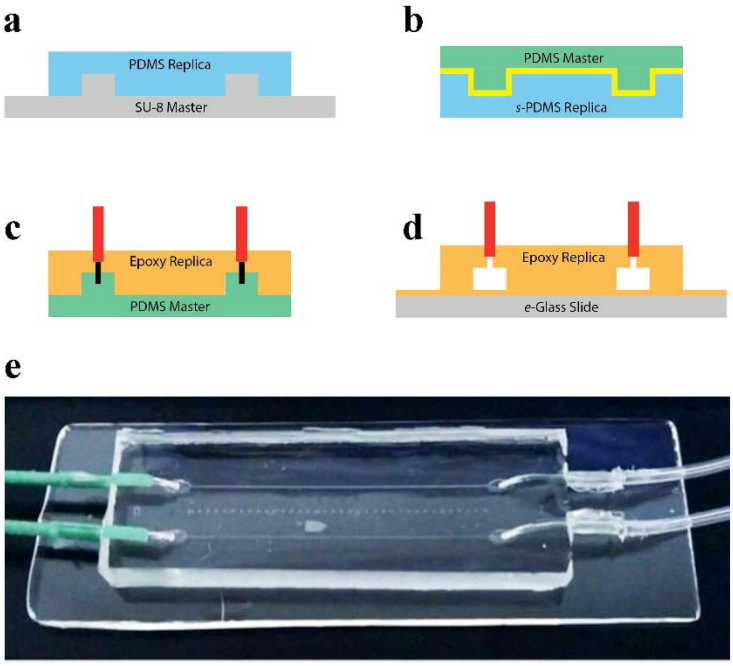

Supplementary Figure 1 | Fabrication of epoxy microchannels. (a) PDMS replica is generated from SU-8 master via soft lithography. **(b)** PDMS master is peeled away from PDMS replica and treated via vapor deposition with (tridecafluoro-1,1,2,2-tetrahydroocttyl) trichlorosilane. **(c)** Epoxy replica is generated from the PDMS master and fitted with Teflon plugs (black) and PEEK or Tygon tubing (red). **(d)** Epoxy replica (with Teflon plugs removed) is bonded to epoxy-coated glass slide. **(e)** Bright-field image of 35-mm long straight channel with 80-μm square cross-section. PEEK tubing is connected to the channel inlet (high-pressure end), and Tygon tubing is connected to the channel outlet (low-pressure end).

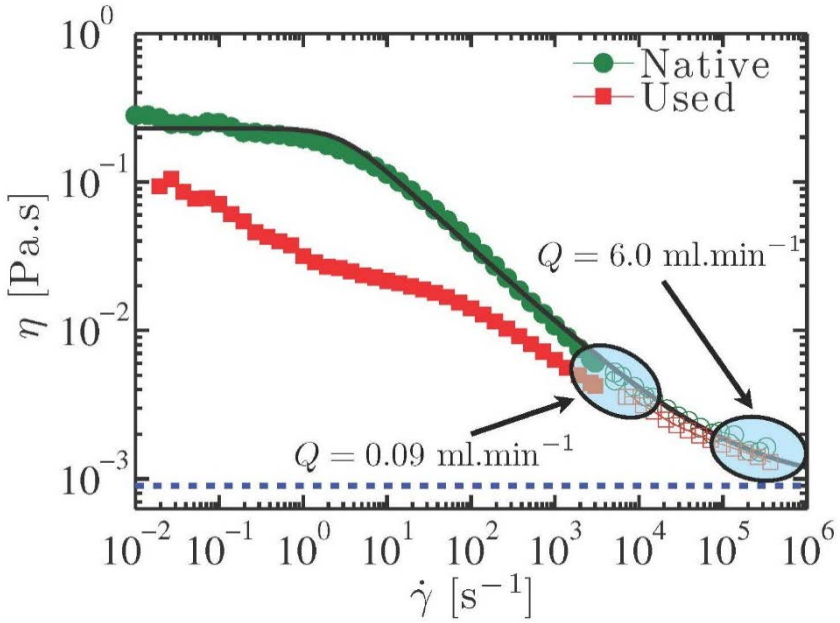

Supplementary Figure 2 | Rheological measurements of HA solutions. Flow curve of HA solution before use ("native") and after use ("used") at flow rates up to Q = 20 ml.min^{-1}. Carreau model fit to unused HA solution, η_0 = 230 mPa.s, η_∞ = 0.9 mPa.s, $\dot{\gamma}^*$ = 0.36 s^{-1}, n = 0.48. Water viscosity (μ_w = 0.9 mPa.s) is shown by blue dashed line.

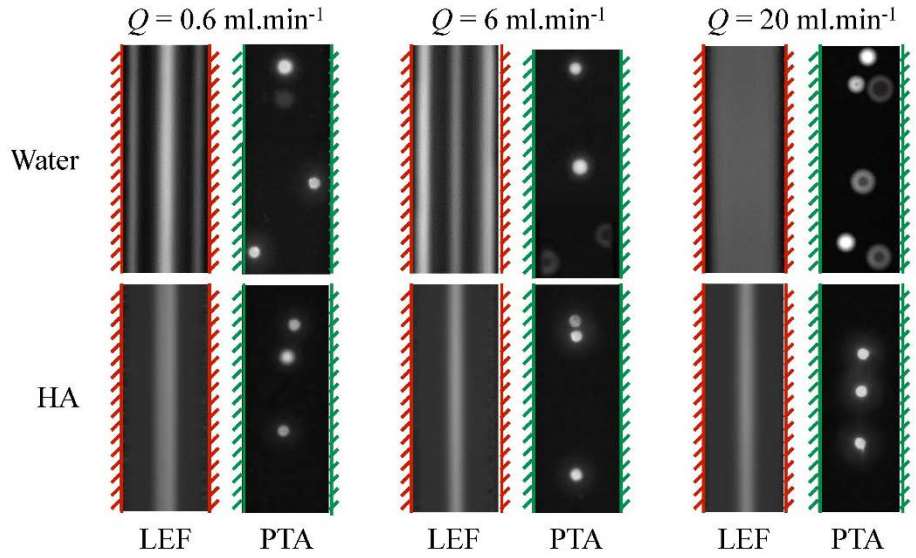

Supplementary Figure 3 | Particle migration behavior in water and HA solution. Long-exposure fluorescence (LEF) characterizes particle focusing behavior based on aggregate signal intensity of particle populations. Particle trajectory analysis (PTA) characterizes particle focusing behavior based on individual particle statistics. The hashed lines indicate the position of the channel walls. At Q = 0.6 ml.min^{-1}, Re = 140 in water, and Re = 105 and Wi = 17 in HA. At Q = 6.0 ml.min^{-1}, Re = 1400 in water, and Re = 1270 and Wi = 170 in HA. At Q = 20.0 ml.min^{-1}, Re = 4360 in water, and Re = 4422 and Wi = 566 in HA.

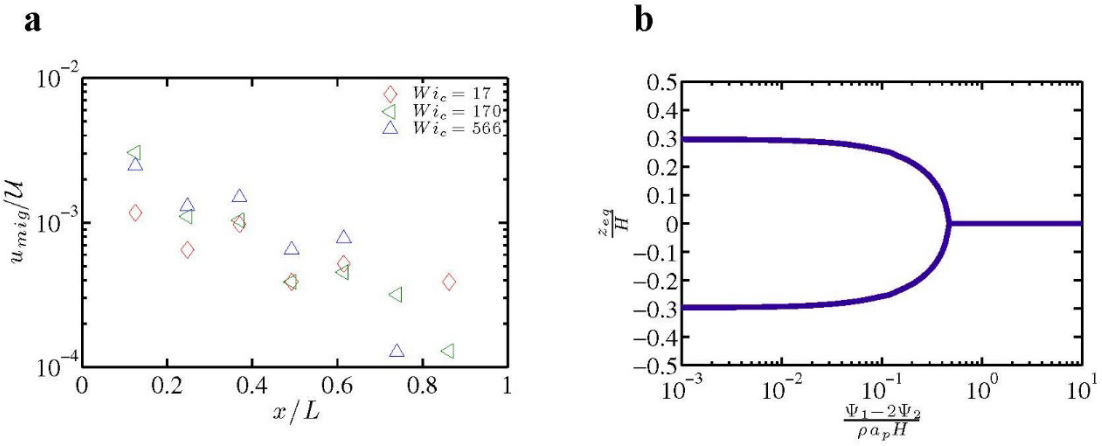

Supplementary Figure 4 | Particle migration dynamics in HA solution. (**a**) Lateral migration velocity of 8-µm particles along the channel length at Q = 0.6, 6 and 20 ml.min^{-1} (U = 1.6, 16 and 52 m.s^{-1}). (**b**) Dimensionless particle equilibrium position z_{eq}/H as a function of the effective elasticity number, calculated using creeping flow theory. The equilibrium migration behavior is increasingly dominated by elasticity for particles of smaller diameter a_p.

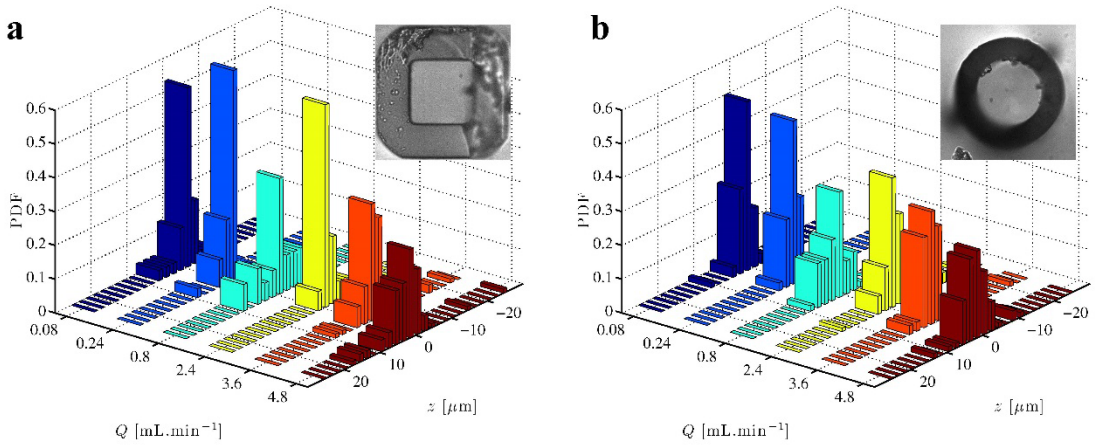

Supplementary Figure 5 | Secondary flow effects in HA solution. Particle distributions across the channel width over a range of flow rates in; **(a)** a borosilicate glass microchannel with square (inner dimension = 50 μm) cross-section, and **(b)** a borosilicate glass microchannel with cylindrical (inner diameter = 50 μm) cross-section. Inset figures show bright-field images of the borosilicate glass microchannels.

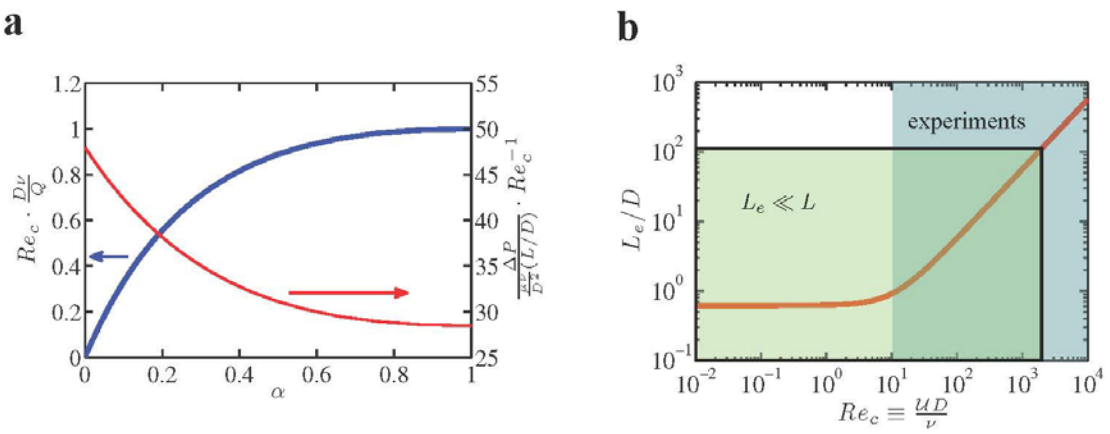

Supplementary Figure 6 | Design parameters for microchannel dimensions. (a) Plot of channel Reynolds number normalized for a constant ratio of *Q*/*D*, and friction factor normalized for a constant value of Re_c as a function of channel aspect ratio $\alpha = W/H$. **(b)** Hydrodynamic entrance length as a function of channel Reynolds number.

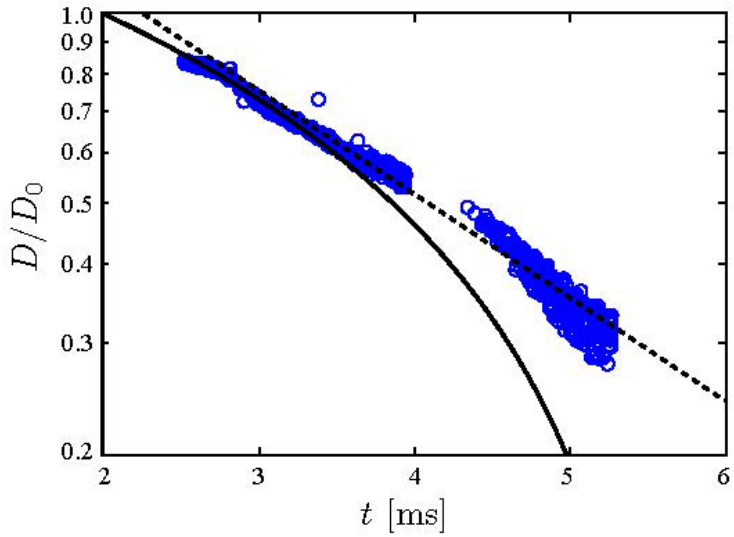

Supplementary Figure 7 | Relaxation time measurement of HA solution. Diameter $D(t)$ of a thinning HA (M_w = 1650 kDa) liquid filament bridge as a function of time t. The dashed line in the figure indicates the initial slope from jetting experiments used to calculate the effective relaxation time. The solid line indicates the visco-capillary break up profile that would be expected if the fluid was a Newtonian fluid. The relaxation time was determined to be $\lambda = 8.7 \times 10^{-4}$ s.

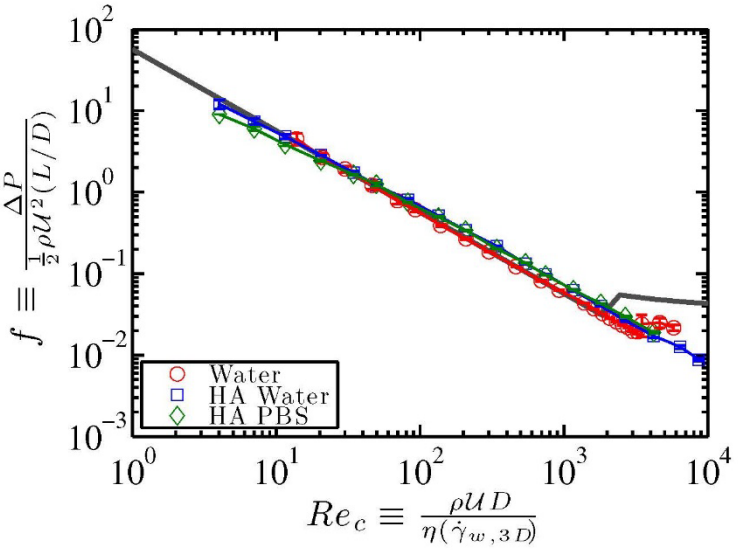

Supplementary Figure 8 | Friction factor in microchannel for Newtonian and viscoelastic fluids. Friction factor *f* as a function of channel Reynolds number Re_c based on a shear rate-dependent viscosity evaluated at the characteristic shear rate at the wall of a microchannel with square cross-section. The gray line indicates the theoretical friction factor for a Newtonian fluid.

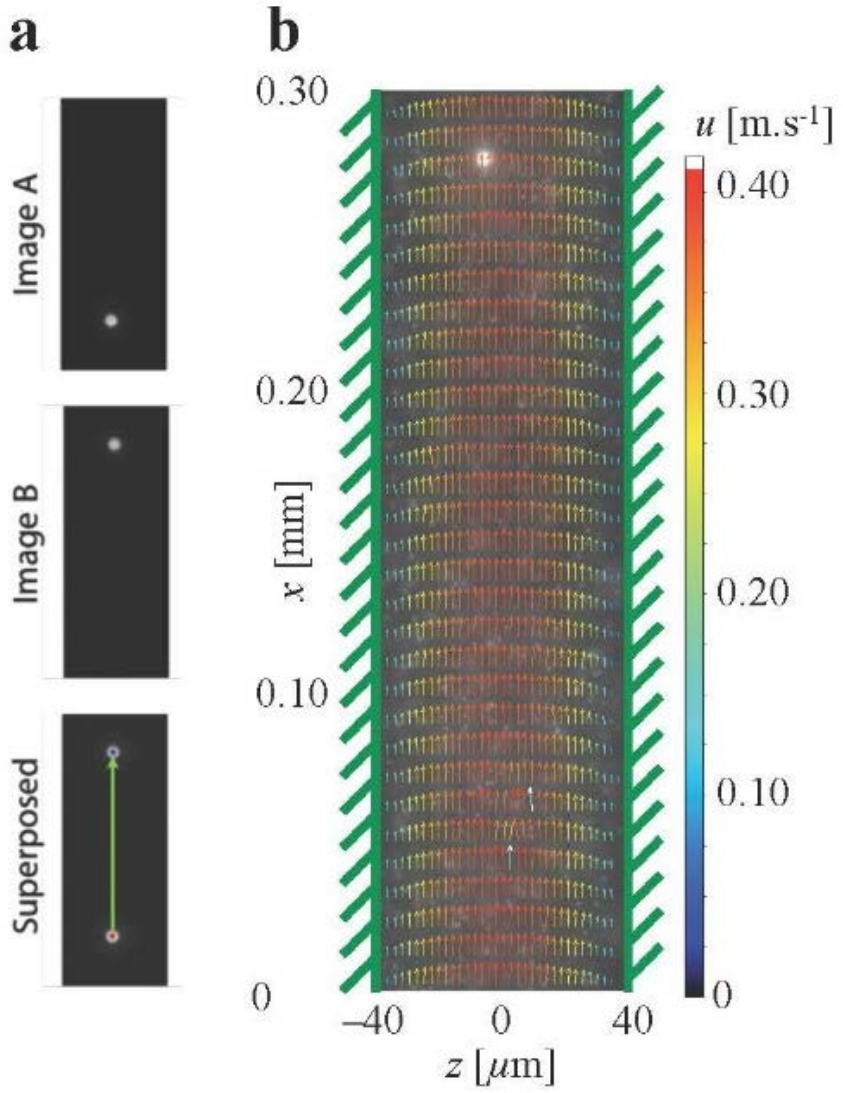

Supplementary Figure 9 | Velocimetry measurements of polystyrene beads in Newtonian and viscoelastic fluids. (a) Representative particle tracking velocimetry (PTV) image pair for determining the velocity of individual 8-μm beads in the microchannel. The exposure time of each frame is δt = 10 ns, and the time interval between Image A and Image B is Δt = 50 μs. **(b)** Representative full-field map of the fluid velocity profile in the microchannel determined from correlative micro particle image velocimetry (μ-PIV) analysis of individual 1-μm beads seeded throughout the fluid sample.

[Supplementary Notes]

Supplementary Note 1 | Lateral Particle Migration and Equilibrium Position. We estimated the lateral particle migration based on the change in the full width at half max (FWHM) of the LEF images captured at Δx = 5-mm intervals along the channel length at Q = 0.6, 6.0 and 20 ml.min^{-1}. The migration velocity is approximately given by $u_{mig} \approx \Delta(\text{FWHM})/2\Delta t$, where $\Delta t = \Delta x/U$ and the factor of two in the denominator results from the fact that particles migrate towards the channel centerline from both sides of the channel. The values of u_{mig} decreased along the channel length (Supplementary Fig. 4a) as the particles asymptotically approach the channel centerline (y,z) = (0,0). The ratio of u_{mig}/U also increased with Q, indicating that at higher Q the particles can reach their equilibrium position using a shorter channel length. Inertial migration in a Newtonian liquid in two-dimensional Poiseuille flow has been treated analytically [1] using the method of reflections. The inertial lift force at the position z in the channel is defined as

$$F_L^I = \frac{81}{8}\left(\frac{a_p}{H}\right)^4 \rho U^2 H^2 \left\{\frac{z}{H}\left[2\frac{z}{H}G_1\left(\frac{z}{H}\right) - G_2\left(\frac{z}{H}\right)\right]\right\} \qquad (1)$$

where G_1 and G_2 are functions of z/H that are determined using the Lorentz reciprocal theorem and must be evaluated numerically to solve for the resulting lift force. When the net inertial lift force on the particle is zero, the particle equilibrates to a position z_{eq}/H = 0.3, which is similar to the dimensionless radial equilibrium position for flow in a pipe found experimentally [2]. Elastic migration in a second order fluid has been studied analytically [3], and the viscoelastic lift force on a particle is defined as

$$F_L^{VE} = -15\pi\frac{a_p^3}{H}\left(\frac{z}{H}\right)(\Psi_1 - 2\Psi_2)\left(\frac{U}{H}\right)^2 \qquad (2)$$

where Ψ_1 and Ψ_2 are the first and second normal stress coefficients of the fluid, respectively. For most viscoelastic liquids $\Psi_1 > -\Psi_2 > 0$, hence the viscoelastic lift force tends to drive a particle towards the channel centerline (*i.e.*, z_{eq} = 0). We simplified this equation by setting $\Psi_1 \sim 2\eta\lambda$ and

$\Psi_2 = 0$ in the main text as expected for a dilute solution from Hookean dumbbell theory [4]. Considerable insight can be gained from these equations to determine the competing effects of inertia and viscoelasticity acting simultaneously on the particle equilibrium position. Equating the two forces to determine the equilibrium position of the particle across the channel width, one obtains the implicit equation

$$2\frac{z_{eq}}{H}G_1\left(\frac{z_{eq}}{H}\right) - G_2\left(\frac{z_{eq}}{H}\right) = \frac{40\pi}{27}\frac{\Psi_1 - 2\Psi_2}{\rho a_p H} \qquad (3)$$

The dimensionless parameter on the right hand side of this equation is a hybrid or *effective elasticity number* that depends on both the channel dimension *H and* the particle diameter a_p. For values of the elasticity number much less than one, inertia dominates and there are multiple equilibrium positions, whereas particles equilibrate along the channel centerline as the elasticity number is increased above $O(1)$ (Supplementary Fig. 4b).

Supplementary Note 2 | Secondary Flow Effects. For microchannels with non-axisymmetric cross-section, normal stress differences in a viscoelastic fluid can drive secondary recirculating flows [5-7]. To observe the effect of secondary flows on particle migration in a viscoelastic fluid, we used borosilicate glass microchannels with round (axisymmetric) or square (non-axisymmetric) cross-section. Particle distributions of 8-μm polystyrene beads in HA solution were obtained using PTA for both microchannels (Supplementary Fig. 5). For a range of channel Reynolds number Re_c corresponding to those studied in the epoxy microchannels, particle focusing toward the channel centerline was observed in both axisymmetric and non-axisymmetric microchannels. At x = 35 mm (which was beyond the equilibrium focusing length L_f), Gaussian fits to the LEF intensity profiles were indistinguishable to within one particle diameter, indicating that secondary flows did not play a significant role.

[Supplementary References]

1. Ho, B. P. & Leal, L. G. Inertial migration of rigid spheres in two-dimensional unidirectional flows. *J. Fluid Mech.* **65,** 365-400 (1974).
2. Segré, G. & Silberberg, A. Radial particle displacements in Poiseuille flow of suspensions. *Nature* **189,** 209-210 (1961).
3. Ho, B. P. & Leal, L. G. Migration of rigid spheres in a two-dimensional unidirectional shear flow of a second-order fluid. *J. Fluid Mech.* **76,** 783-799 (1976).
4. Bird, R. B., Armstrong, R. C. & Hassager, O. *Dynamics of Polymeric Systems: Fluid Mechanics* (John-Wiley & Sons, 1987).
5. Xue, S. C., Phan-Thien, N. & Tanner, R. I. Numerical study of secondary flows of viscoelastic fluid in straight pipes by an implicit finite volume method. *J. Non-Newtonian Fluid Mech.* **59,** 191-213 (1995).
6. Zrehen, A. & Ramachandran, A. Demonstration of secondary currents in the pressure-driven flow of a concentrated suspension through a square conduit. *Phys. Rev. Lett.* **110,** 018306 (2013).
7. Villone, M. M., D'Avino, G., Hulsen, M. A., Greco, E. F. & Maffettone, P. L. Particle motion in square channel flow of a viscoelastic liquid: migration vs. secondary flows. *J. Non-Newtonian Fluid Mech.* **195,** 1-8 (2013).